NASA/TP-2015-218980

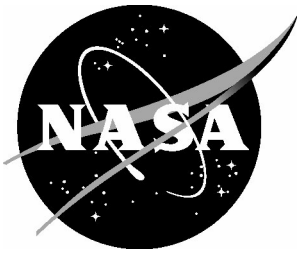

Solar Proton Transport within an ICRU Sphere Surrounded by a Complex Shield: Combinatorial Geometry

John W. Wilson
Old Dominion University, Norfolk, Virginia

Tony C. Slaba
Langley Research Center, Hampton, Virginia

Francis F. Badavi
Old Dominion University, Norfolk, Virginia

Brandon D. Reddell and Amir A. Bahadori
Johnson Space Center, Houston, Texas

November 2015

NASA STI Program . . . in Profile

Since its founding, NASA has been dedicated to the advancement of aeronautics and space science. The NASA scientific and technical information (STI) program plays a key part in helping NASA maintain this important role.

The NASA STI program operates under the auspices of the Agency Chief Information Officer. It collects, organizes, provides for archiving, and disseminates NASA's STI. The NASA STI program provides access to the NTRS Registered and its public interface, the NASA Technical Reports Server, thus providing one of the largest collections of aeronautical and space science STI in the world. Results are published in both non-NASA channels and by NASA in the NASA STI Report Series, which includes the following report types:

- TECHNICAL PUBLICATION. Reports of completed research or a major significant phase of research that present the results of NASA Programs and include extensive data or theoretical analysis. Includes compilations of significant scientific and technical data and information deemed to be of continuing reference value. NASA counter-part of peer-reviewed formal professional papers but has less stringent limitations on manuscript length and extent of graphic presentations.

- TECHNICAL MEMORANDUM. Scientific and technical findings that are preliminary or of specialized interest, e.g., quick release reports, working papers, and bibliographies that contain minimal annotation. Does not contain extensive analysis.

- CONTRACTOR REPORT. Scientific and technical findings by NASA-sponsored contractors and grantees.

- CONFERENCE PUBLICATION. Collected papers from scientific and technical conferences, symposia, seminars, or other meetings sponsored or co-sponsored by NASA.

- SPECIAL PUBLICATION. Scientific, technical, or historical information from NASA programs, projects, and missions, often concerned with subjects having substantial public interest.

- TECHNICAL TRANSLATION. English-language translations of foreign scientific and technical material pertinent to NASA's mission.

Specialized services also include organizing and publishing research results, distributing specialized research announcements and feeds, providing information desk and personal search support, and enabling data exchange services.

For more information about the NASA STI program, see the following:

- Access the NASA STI program home page at http://www.sti.nasa.gov

- E-mail your question to help@sti.nasa.gov

- Phone the NASA STI Information Desk at 757-864-9658

- Write to:
  NASA STI Information Desk
  Mail Stop 148
  NASA Langley Research Center
  Hampton, VA 23681-2199

NASA/TP-2015-218980

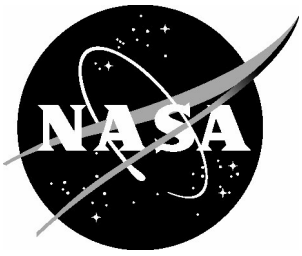

Solar Proton Transport within an ICRU Sphere Surrounded by a Complex Shield: Combinatorial Geometry

John W. Wilson
Old Dominion University, Norfolk, Virginia

Tony C. Slaba
Langley Research Center, Hampton, Virginia

Francis F. Badavi
Old Dominion University, Norfolk, Virginia

Brandon D. Reddell and Amir A. Bahadori
Johnson Space Center, Houston, Texas

National Aeronautics and
Space Administration

Langley Research Center
Hampton, Virginia 23681-2199

November 2015

Available from:

NASA STI Program / Mail Stop 148
NASA Langley Research Center
Hampton, VA 23681-2199
Fax: 757-864-6500

Contents

Figures

Tables

Abstract

The 3DHZETRN code, with improved neutron and light ion ($Z \leq 2$) transport procedures, was recently developed and compared to Monte Carlo (MC) simulations using simplified spherical geometries. It was shown that 3DHZETRN agrees with the MC codes to the extent they agree with each other. In the present report, the 3DHZETRN code is extended to enable analysis in general combinatorial geometry. A more complex shielding structure with internal parts surrounding a tissue sphere is considered and compared against MC simulations. It is shown that even in the more complex geometry, 3DHZETRN agrees well with the MC codes and maintains a high degree of computational efficiency.

Introduction

A 3D version of HZETRN has recently been developed and tested in simple geometries and compared to available Monte Carlo (MC) codes [Wilson et al. 2014a-c, 2015]. In the first study [Wilson et al. 2014a,b], an aluminum sphere with a radial thickness of 20 g/cm^2 was examined, and comparisons were made between 3DHZETRN results and MC simulations at locations within the sphere exposed to solar particle event (SPE) and galactic cosmic ray (GCR) boundary conditions. Well defined convergence tests were performed that spanned the transport formalism, covering the straight ahead approximation ($N = 1$), bi-directional approximation ($N = 2$), and more detailed 3D treatment ($N > 2$) for neutrons and light ions. Note that in the formalism of Wilson et al. [2014a-c, 2015], N denotes the number of transport directions used to describe the assumed isotropic neutron and light ion fluxes at lower energies. The convergence tests and comparison to MC results established improved description of the neutron and light ion solutions within the 3D formalism. It was also shown that although there are still noticeable differences associated with the nuclear production models used in the codes, 3DHZETRN agreed with the MC models to the extent they agree with each other in finite geometry. The main difference between the transport codes was found to be in the computational costs. While 3DHZETRN results were generated in several seconds on a single CPU, the MC code run times were several orders of magnitude larger (~10^8 seconds) and required high performance computing clusters.

In the next study [Wilson et al. 2014c, 2015], a tissue sphere with a radial thickness of 15 g/cm^2, defined by the International Commission on Radiation Units and Measurements (ICRU) [ICRU 1993], was surrounded by an aluminum spherical shell with thickness 20 g/cm^2, and similar convergence tests and comparisons to MC were provided. Improvements in the low energy neutron and light ion spectra as a result of 3D corrections were again clearly established. Despite the added geometric complexity of the two material sphere configuration, agreement between all the codes was actually improved compared to the previous single material aluminum sphere. The improved agreement was attributed to the hydrogen content of the ICRU tissue sphere. For energies below ~100 MeV, elastic collisions between neutrons and hydrogen dominate the neutron transport processes. These elastic collisions, on average, transfer half the neutron energy to the target hydrogen, which in turn, very rapidly attenuates the neutron energy spectrum. Although neutron production cross sections show significant variation amongst the codes for aluminum targets, as seen in the first study [Wilson et al. 2014a,b], neutron-hydrogen elastic cross sections are more precisely and accurately represented in the codes either through evaluated nuclear data files or detailed parameterizations [Wilson et al. 1991]. Again, it was found that 3DHZETRN was in good agreement with the MC simulation results, and the primary difference between the codes lay in the associated computational costs, where 3DHZETRN is several orders of magnitude faster.

Herein, a more complex and realistic shielding geometry with multiple parts is considered. An ICRU tissue sphere is surrounded by a cylindrical aluminum shell containing two additional internal aluminum boxes. The sizes and locations of the internal parts are chosen to provide partial shielding of the ICRU sphere, thereby emphasizing 3D effects in the transport process. The chosen geometry is sufficiently complex to further test 3DHZETRN while still allowing engagement of various MC codes to verify the solution methods.

In this report, transport code development efforts will be briefly reviewed with an emphasis on the most recent extensions leading to a generalized version of 3DHZETRN applicable in combinatorial geometry. As in the previous studies [Wilson et al. 2014a-c, 2015], convergence tests are performed and comparison to MC simulations are provided. The next step in 3DHZETRN development will allow the use of more complex and realistic geometric models, including human phantoms, so that simple mapping of the present methodology into more realistic applications can be studied. Although a final solution to engineering design problems is not yet at hand, the current status of deterministic methods agrees with MC codes to the degree that various MC codes agree among themselves

in many cases. The main limitation within 3DHZETRN remains in the nuclear databases and requires additional experimental measurements and nuclear model development.

3DHZETRN

The 3DHZETRN theoretical formalism has been provided in prior reports [Wilson et al. 2014a-c, 2015] and will not be repeated in detail here. However, an overview is given here to provide clarity in the notation and terminology used later in this paper. Additional discussion is given in this section regarding extensions of the present code to general combinatorial geometry.

Theoretical Formalism Overview

The linear Boltzmann transport equation within the continuous slowing down approximation for the flux (or fluence) density, $\phi_j(\boldsymbol{x},\boldsymbol{\Omega},E)$, of a *j* type particle is given by [Wilson et al. 1991, 2005]

$$\mathbf{B}[\phi_j(\boldsymbol{x},\boldsymbol{\Omega},E)] = \sum_k \int_E^\infty \int_{4\pi} \sigma_{jk}(E,E',\boldsymbol{\Omega},\boldsymbol{\Omega}')\phi_k(\boldsymbol{x},\boldsymbol{\Omega}',E')\,d\boldsymbol{\Omega}'\,dE'\,, \tag{1}$$

where the differential operator on the left hand side is defined as

$$\mathbf{B}[\phi_j(\boldsymbol{x},\boldsymbol{\Omega},E)] \equiv \boldsymbol{\Omega}\bullet\nabla\phi_j(\boldsymbol{x},\boldsymbol{\Omega},E) - \frac{1}{A_j}\frac{\partial}{\partial E}\left[S_j(E)\phi_j(\boldsymbol{x},\boldsymbol{\Omega},E)\right] + \sigma_j(E)\phi_j(\boldsymbol{x},\boldsymbol{\Omega},E)\,. \tag{2}$$

In equations (1) and (2), A_j is the atomic mass of a type *j* particle, $S_j(E)$ is the stopping power of a type *j* ion with kinetic energy *E* (vanishes for neutrons), $\sigma_j(E)$ is the total macroscopic cross section for a type *j* particle with kinetic energy *E*, and $\sigma_{jk}(E,E',\boldsymbol{\Omega},\boldsymbol{\Omega}')$ is the double differential macroscopic production cross section for interactions in which a type *k* particle with kinetic energy *E*' and direction $\boldsymbol{\Omega}'$ produce a type *j* particle with kinetic energy *E* and direction $\boldsymbol{\Omega}$.

Solution methods are developed by separating the double differential cross section for neutron ($j = n$) production and the particle fluxes into forward and isotropic components. The forward components are associated mainly with higher energy direct quasi-elastic events and projectile fragmentation products [Wilson 1977, Wilson et al. 1988], and the isotropic components are associated with lower energy secondary particles, including target fragments.

The forward component is first solved within the straight ahead approximation, wherein all particles are assumed to travel along a common axis ($\boldsymbol{\Omega} \approx \boldsymbol{\Omega}'$). This allows previously developed and highly efficient numerical solution techniques to be utilized [Wilson et al. 1991, Slaba et al. 2010a]. The forward solution then gives rise to a source of isotropically produced neutrons, given as

$$\xi_{n,iso}(\boldsymbol{x},\boldsymbol{\Omega},\boldsymbol{\Omega}_0,E) = \sum_k \int_E^\infty \sigma_{nk,iso}(E,E',\boldsymbol{\Omega},\boldsymbol{\Omega}_0)\phi_{k,for}(\boldsymbol{x},\boldsymbol{\Omega}_0,E')\,dE'\ , \tag{3}$$

where $\sigma_{nk,iso}(E,E',\boldsymbol{\Omega},\boldsymbol{\Omega}')$ is the isotropic component of the neutron production cross section, and $\phi_{k,for}(\boldsymbol{x},\boldsymbol{\Omega},E')$ is the forward component of the flux. The symbol $\boldsymbol{\Omega}_0$ denotes the direction of the inbound forward flux arriving at location $\boldsymbol{x}$, and $\boldsymbol{\Omega}$ denotes the transport direction within the geometry along which the isotropic flux is being computed, as in Fig. 1. The transport equation for the isotropic neutron flux is given by

$$\begin{aligned}[\boldsymbol{\Omega}\bullet\nabla + \sigma_n(E)]\phi_{n,iso}(\boldsymbol{x},\boldsymbol{\Omega},E) = &\int_E^\infty \int_{4\pi} \sigma_{nn}(E,E',\boldsymbol{\Omega},\boldsymbol{\Omega}')\phi_{n,iso}(\boldsymbol{x},\boldsymbol{\Omega}',E')\,d\boldsymbol{\Omega}'\,dE' \\ &+\xi_{n,iso}(\boldsymbol{x},\boldsymbol{\Omega},\boldsymbol{\Omega}_0,E)\end{aligned}\,. \tag{4}$$

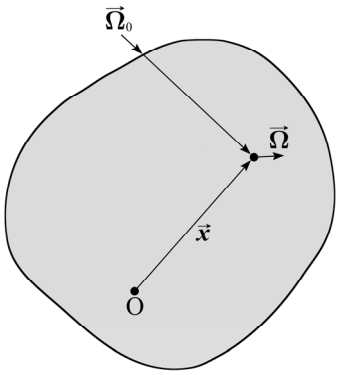

Fig. 1. Geometry depicting relationship between the forward direction $\mathbf{\Omega}_0$ and transport direction $\mathbf{\Omega}$ at location $\boldsymbol{x}$.

Equation (4) is solved along the transport direction $\mathbf{\Omega}$ within the bi-directional approximation discussed in detail elsewhere [Slaba et al. 2010b]. A final step in the solution methodology is to compute the source of light ions produced from the lower energy isotropic neutrons. Once this source is computed, the isotropic component of the light ion flux is solved under the assumption that no further nuclear collisions occur, giving partial 3D treatment to low energy charged particles.

A remaining detail in the transport formalism is to define a discrete number, N, of transport directions, $\mathbf{\Omega}$, over which the isotropic flux is evaluated. In connecting to historical code development, the $N = 1$ solution corresponds to the usual straight ahead approximation wherein all particles are assumed to follow a common axis. In this case, there is only one transport direction $\mathbf{\Omega}$, and $\mathbf{\Omega} = \mathbf{\Omega}_0$. The $N = 2$ solution corresponds to the bi-directional transport approximation, wherein particles are allowed to propagate either straight forward or straight backward. In this case, there are two transport directions ($\mathbf{\Omega}_1 = \mathbf{\Omega}_0$ and $\mathbf{\Omega}_2 = -\mathbf{\Omega}_0$). Values of $N > 2$, correspond to a more detailed three dimensional (3D) description of the isotropic flux component and are the emphasis of recent advances in code development [Wilson et al 2014a-c, 2015]. In those previous studies, values of $N = 1, 2, 6, 10, 14, 18, 22$ were considered, as shown in Fig. 2.

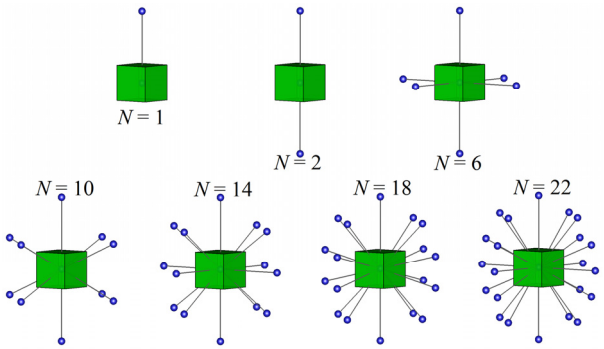

Fig. 2. Transport directions used to describe isotropic component of flux.

These distributions were developed by prescribing a number of latitudinal (N_α) and longitudinal (N_β) directions along with the two polar directions. For the present study, a generalized algorithm for computing the transport direction vectors, $\mathbf{\Omega}$, was implemented into the code to enable more comprehensive testing in complex geometry, as will be shown in the next section.

The algorithm is described as follows. The number of latitudinal (N_α) and longitudinal (N_β) directions is chosen. This gives the total number of directions

$$N = N_\alpha N_\beta + 2, \tag{5}$$

where the two additional polar directions (forward/backward) have been added. The longitudinal angles (β_i) and latitudinal angles (α_i) are computed as

$$\beta_i = 2\pi \frac{i-1}{N_\beta}, \tag{6}$$

$$\alpha_i = \arccos\left[a + \frac{\Delta}{2}(2i-1)\right], \tag{7}$$

where $a = -1 + 2 / N$, $b = 1 - 2 / N$, and $\Delta = (b-a) / N_\alpha$. The directional components are then computed using the typical spherical coordinate transformations

$$\mathbf{\Omega}_i = \begin{pmatrix} \cos(\beta_i)\sin(\alpha_i) \\ \sin(\beta_i)\sin(\alpha_i) \\ \cos(\alpha_i) \end{pmatrix}. \tag{8}$$

In the following section, convergence in the induced radiation field within the ICRU tissue sphere is examined as a function of *N*, and transport direction distributions as large as $N = 86$ are considered.

Combinatorial Geometry

The present work required extensions to 3DHZETRN to enable general combinatorial geometry to be studied. As a result, an efficient computational ray-tracer was developed and integrated into the code. Fundamentally, the ray-tracer provides the thickness and type of each material traversed in moving from any location in space along an arbitrary direction through the geometry. Such information is required in two places within the 3DHZETRN formalism (see Fig. 1). First, to evaluate the forward flux along the direction $\mathbf{\Omega}_0$, the ray-tracer provides the ordering, material types, and thicknesses traversed in passing from the outermost geometric boundary to the point of interest, $\boldsymbol{x}$. Second, to evaluate the isotropic flux along the transport direction $\mathbf{\Omega}$ passing through $\boldsymbol{x}$, the ray-tracer is called again to provide similar information.

Solid spheres, boxes, cylinders, and ellipsoids can be easily ray-traced since the equations describing intersection between any ray in space and one of the solids have a closed form analytic solution. Additional geometric and computational complexity is introduced when these simple solids are nested inside each other but must be included as a capability.

The currently implemented ray-tracer allows any number of the simple solids to be nested inside each other, allowing relatively complex geometries to be defined. Partially nested solids (i.e. solids that are not entirely contained by another solid) are not currently supported. Nesting geometric solids is achieved computationally by requiring simple containment (mother-daughter) relationships to be explicitly defined prior to execution. In particular, the definition of each object prior to execution includes a field identifying its immediate mother volume (i.e. the solid that contains it). From this basic information, a complete mother-daughter tree is generated within the code for the ray-tracer upon execution.

The overall procedure of the ray-tracer is described as follows. For a given point and ray-trace direction, intersection distances between the point and the boundaries of each solid in the geometry are computed. If no intersection with a given solid occurs, the evaluated distance is set as a negative number. Next, the list of intersection distances is sorted from smallest to largest. This sets the ordering of objects and materials traversed along the ray. Negative numbers in the list, corresponding to solids that were not intersected, are discarded. The remaining list of intersection distances uniquely defines the ordering, material types, and lengths traversed by the ray and is then passed from the ray-tracer to the transport procedure.

The present status of the ray-tracer allows relatively complex shielding geometries to be efficiently studied within the 3DHZETRN transport code. Future work will describe implementation of detailed human phantom models into the code. Also, extensions to the ray-tracer to enable compatibility with shielding thickness distributions, as generated in the computer aided design vehicle optimization analyses, are forthcoming. Both of these advancements will provide the final connections between the computationally efficient 3DHZETRN code to engineering design and radiation risk studies for space applications.

Complex Inhomogeneous Geometry

As in prior studies, geometry of sufficient simplicity will be chosen to allow MC simulation using available computer resources in a reasonable commitment of time but of sufficient complexity to allow testing of the 3DHZETRN procedures. The geometry under consideration is shown in Fig. 3. A 30 cm diameter tissue equivalent sphere [ICRU 1993] is placed within a 2.47 cm (5 g/cm^2) thick cylindrical aluminum shell (outer diameter 75 cm, outer length 175 cm) with 4.9 cm (10 g/cm^2) thick end caps. In addition to the ICRU sphere at the center of the aluminum cylindrical shell, an interior aluminum box with dimensions 46.3×14.8×14.8 cm (upper right corner in Fig. 3) and a second aluminum box with dimensions 22.2×22.2×37.0 cm (lower left corner in Fig. 3) are also placed inside the cylinder. The dimensions of these boxes in units of g/cm^2 are 125×40×40 and 60×60×100, respectively. Target points (detectors) are placed within the ICRU tissue sphere, similar to the previous study [Wilson et al. 2014c, 2015]. The detector locations appearing at the top and bottom of the ICRU tissue sphere will be referred to in subsequent figures, tables, and discussion as $z = 0$ and $z = 30$, respectively. Additional target points within the ICRU tissue sphere are therefore defined by their location between the top and bottom detectors. For example, the detector location in the center of the sphere is referred to as $z = 15$.

The external radiation environment (external source boundary condition) is positioned above the geometry and directed uniformly downward along $\mathbf{\Omega}_0$ as indicated by the arrows in Fig. 3. For all calculations, the boundary condition, or external source, is the Webber representation of the February 23, 1956 solar particle event (SPE) [Webber 1966]. The Webber 1956 SPE is given by an exponential momentum spectrum with momentum parameter $p_0 = 100$ MV and 10^9 protons/cm^2 above 30 MeV.

An important feature of the complex geometry is the partial shielding of the ICRU tissue sphere provided by the internal aluminum boxes. In particular, the box in the upper right corner casts a shadow onto part of the tissue sphere as shown in Fig. 4. Note that similar effects were also shown in a prior study [Wilson et al. 2014c, 2015] for various external boundary conditions but in simpler geometry. Fig. 4 shows the source of neutrons induced by the Webber SPE event within the complex geometry computed with 3DHZETRN. The rapid attenuation of the neutron source intensity along the direction of the incident SPE protons, $\mathbf{\Omega}_0$, is evident, as is the shadow cast by the upper right aluminum box onto the tissue sphere. The added complexity of the non-uniformly shielded and partially shadowed tissue sphere should accentuate 3D transport processes and provide a more rigorous test for the 3DHZETRN model.

The neutron fluence at a point within the sphere depends not only on the distance to the boundary along a given transport direction, $\mathbf{\Omega}$, but also on the intensity of the source along $\mathbf{\Omega}$ in reaching the boundary. The most intense regions of the neutron source must be adequately represented in the domain of the numerical solution. This requires sufficient fidelity in the set of transport directions, $\mathbf{\Omega}$, as defined by equations (5) - (8) in the previous section. The convergence rate for increasing number of N will be tested in the following section.

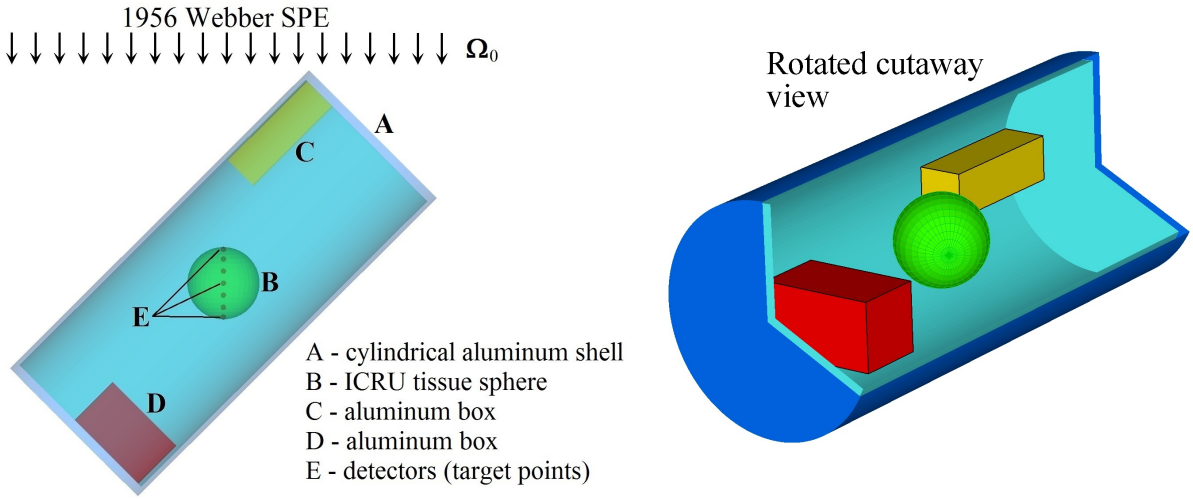

Fig. 3. Complex geometry used in the current study: ICRU tissue sphere shielded by an aluminum cylindrical shell with internal parts.

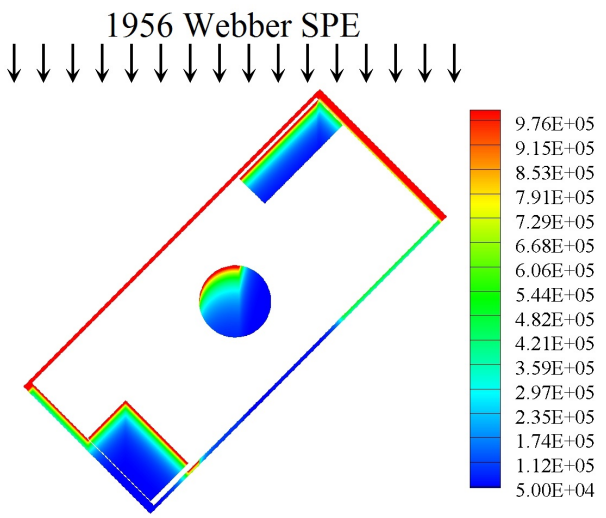

Fig. 4. Integral ($E > 1$ MeV) isotropic neutron source (particles/(g-event)) induced by the Webber SPE incident on an ICRU sphere shielded by a complex aluminum structure.

Preliminary testing

A convergence study was made to examine the solution dependence on the number of longitudinal nodes, N_β, and latitudinal nodes, N_α, used to define the set of transport directions, $\mathbf{\Omega}$. For this convergence test, the quantity studied is dose equivalent at the bottom of the ICRU sphere, since it is typically a more sensitive measure than dose. The solution with $N = 86$ ($N_\beta = 12$, $N_\alpha = 7$) is taken as the converged solution, and the relative error over a range of values is shown in Fig. 5.

By comparing recent studies [Wilson et al 2014a-c, 2015], it can be seen that the convergence behavior depends on the shape and complexity of the shield geometry, as would be expected. For example, in those prior studies, results computed in spherical shielding converged well with $N = 18$ and above. In the present set of results, it can be seen that relative error less than 3% is achieved for $N_\alpha > 4$ and $N_\beta > 5$.

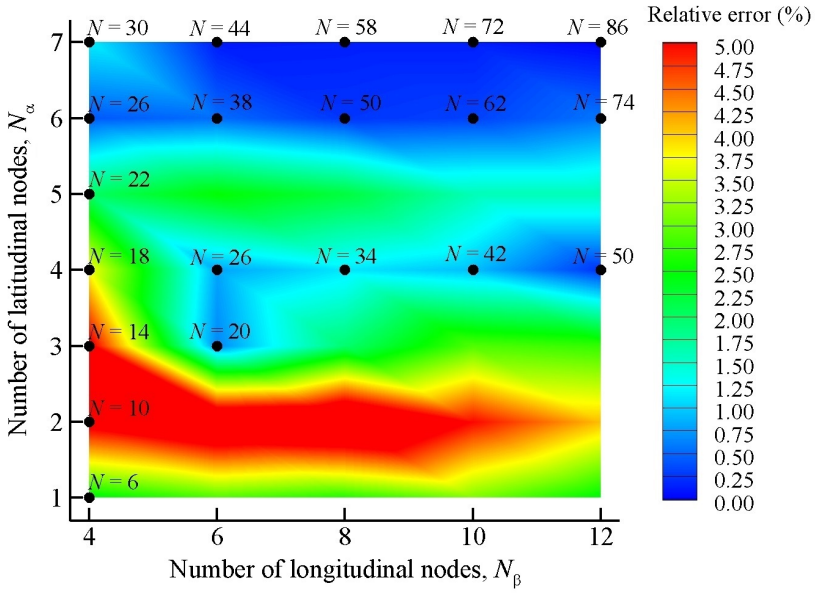

Fig. 5. Relative error (%) in dose equivalent at the $z = 30$ detector location (bottom of the ICRU sphere).

Also of interest is the dose and dose equivalent at locations within the tissue sphere. Dosimetric quantities are evaluated at depths in the tissue sphere at z = {0, 0.007, 0.3, 1, 5, 25, 29, 29.7, 29.993, 30} g/cm^2 with results in Tables 1 and 2 for N = 1, 2, 6, 10, 26, 38, 58, 86. The doses near the top and bottom of the tissue sphere are seen to converge rapidly with increasing N. The local fields in these locations are dominated by transport through the aluminum shield giving improved convergence behavior over the case concerning the surface of a homogeneous aluminum shield [Wilson et al. 2014a,b]. The rate of convergence of dose equivalent is somewhat slower, since the details on the penetration of charged particles produced by neutrons are more dependent on angular factors. Still, the rate of convergence is quite rapid in the complex geometry with adequate results in only 20 or more transport directions (see Fig. 5), similar to the spherical shell shield studied in earlier papers [Wilson et al. 2014c,2015].

The solution methodology appears to be nearly converged for N > 20. This is supported in Tables 1 and 2 by comparing exposure values for different N at a fixed depth. The relative difference, compared to the N = 86 solution, is found to be less than 1% for dose and less than 2% for dose equivalent for N > 10 at all depths. The induced particle fluence is shown in Fig. 6 at the near (z = 0) and distal (z = 30) interfaces. Also shown are the lowest order N = 1 and N = 2 solutions, corresponding to the straight ahead and bi-directional approximations, respectively. The N = 1 solution has no contributions from the backward leaking neutrons that have been moderated within the tissue sphere. This can be seen in the incorrect neutron spectral shape below 20 MeV at z = 0. This error is largely corrected by the N = 2 bi-directional approximation. All solutions are nearly converged for N > 10 (i.e. within fractions of a percent of the N = 86 result).

Table 1. Webber SPE dose as a function of number of transport directions, N, at various depths in the tissue sphere including those defined by ICRU.

z (g/cm^2)	Dose (cGy/event)							
	N = 1	N = 2	N = 6	N = 10	N = 26	N = 38	N = 58	N = 86
0	42.76	42.78	42.76	42.80	42.79	42.79	42.78	42.78
0.007	42.46	42.48	42.47	42.49	42.49	42.48	42.48	42.48
0.3	38.68	38.76	38.74	38.76	38.75	38.75	38.74	38.75
1	32.32	32.40	32.38	32.40	32.39	32.38	32.38	32.38
5	14.56	14.61	14.59	14.61	14.59	14.59	14.59	14.59
25	1.55	1.55	1.54	1.54	1.55	1.54	1.55	1.54
29	1.13	1.13	1.13	1.12	1.13	1.13	1.13	1.13
29.7	1.08	1.07	1.08	1.06	1.07	1.07	1.07	1.07
29.993	1.05	1.05	1.05	1.04	1.05	1.05	1.05	1.05
30	1.05	1.05	1.03	1.03	1.04	1.04	1.04	1.04

Table 2. Webber SPE dose equivalent as a function of number of transport directions, N, at various depths in the tissue sphere including those defined by the ICRU.

z (g/cm^2)	Dose Equivalent (cSv/event)							
	N = 1	N = 2	N = 6	N = 10	N = 26	N = 38	N = 58	N = 86
0	65.90	65.99	65.69	66.08	65.99	65.94	65.86	65.90
0.007	62.51	62.56	62.37	62.62	62.51	62.44	62.41	62.45
0.3	54.92	55.49	55.26	55.47	55.36	55.28	55.26	55.31
1	45.73	46.27	46.06	46.24	46.15	46.06	46.04	46.09
5	20.68	21.03	20.81	20.94	20.81	20.76	20.78	20.82
25	2.64	2.63	2.56	2.47	2.59	2.57	2.58	2.57
29	2.03	2.00	2.04	1.90	2.04	2.02	2.05	2.05
29.7	1.95	1.91	2.00	1.83	1.98	1.96	1.99	1.99
29.993	1.91	1.86	1.99	1.79	1.94	1.91	1.96	1.95
30	1.91	1.84	1.80	1.74	1.85	1.83	1.84	1.84

The fluence spectra in the neighborhood of the near and distal interface are shown in Fig. 7 for N = 26. A rapid transition occurs in passing from aluminum to tissue in the near interface and in passing from tissue to aluminum in the distal interface. This can be seen in the proton and ^{4}He spectra in Fig. 7 below 10 MeV/n. The ^{4}He fluence spectra are shown in the neighborhood of the near and distal interfaces on an expanded scale in Fig. 8. The

^{4}He ions produced in the aluminum shield rapidly form a new equilibrium spectrum within the first few millimeters of tissue as observed in the near interface. Similarly, at the distal interface, the leakage of ^{4}He from the aluminum into the tissue shield quickly forms a new, less dynamic, approach to an equilibrium spectrum within the first few millimeters of tissue.

One difference for the present complex inhomogeneous geometry compared to the tissue sphere in close contact with the aluminum spherical shell [Wilson et al. 2014c, 2015] is that the aluminum surface in the present case is exposed to the secondary light ions over a restricted solid angle whereas the spherical shell configuration is over the full hemisphere. This results in some differences in behavior in the transition region. This is seen most clearly by comparing the present result in Fig. 8 with the results derived previously for the inhomogeneous sphere [Wilson et al. 2014c, 2015].

It is found that the details of the ^{4}He spectra (for example, see Fig. 8) cannot be verified by MC simulations since the computational costs required to control statistical fluctuations at low energies are too large. Even the hope of defining the transition regions for neutrons and protons has not been successful in MC simulations. Biasing techniques could be implemented to resolve these issues in future work. As a result, the larger features generated from MC simulations are used to verify the 3DHZETRN results. If the trends in the 3DHZETRN solution over larger distances are verified, then it is reasonably assumed that the interface details revealed by 3DHZETRN are reasonably correct in the context of the current interaction models. The N = 26 will be used in the MC benchmarks discussed in the next section.

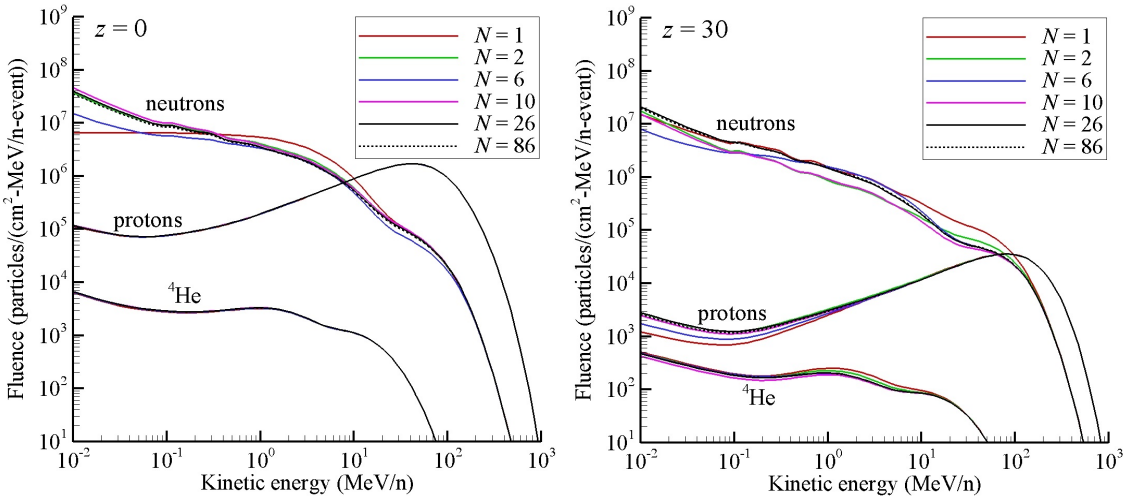

Fig. 6. Webber SPE convergence test at the top (left plot) and bottom (right plot) of a 30 g/cm^2 diameter tissue sphere within a complex shield of aluminum.

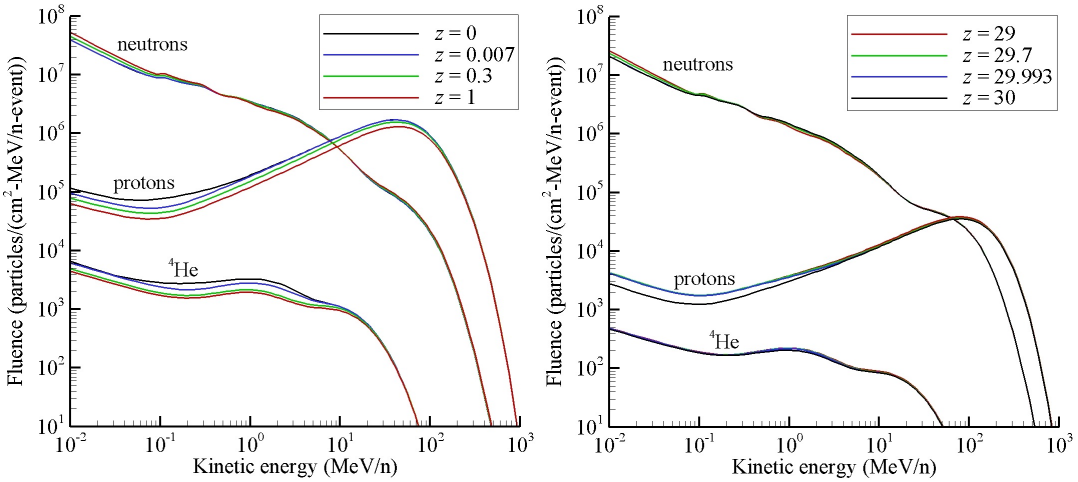

Fig. 7. Webber SPE induced fluence within the ICRU sphere at locations near the top (left plot) and bottom (right plot) tissue/shield interface with N = 26.

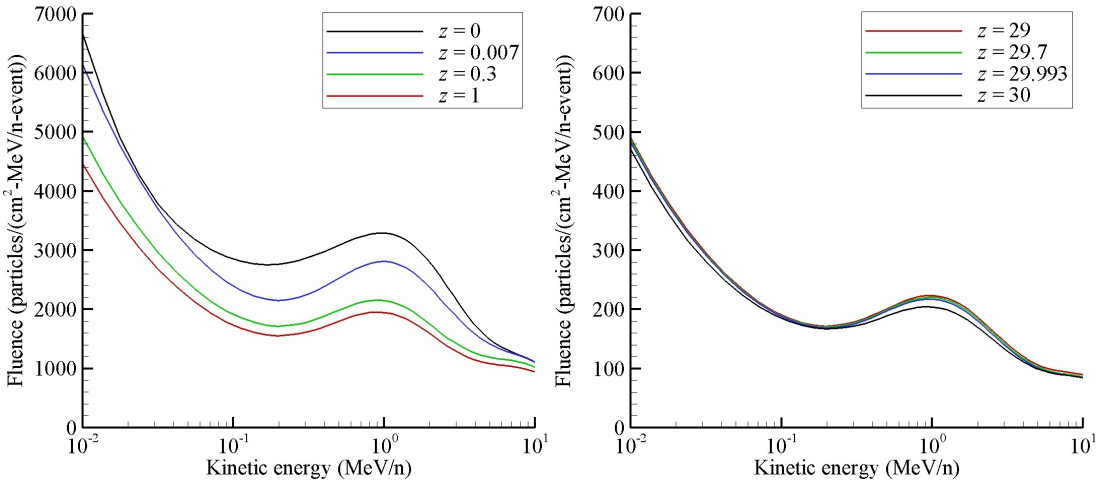

Fig. 8. Webber SPE induced ^{4}He fluence within the ICRU sphere at locations near the top (left plot) and bottom (right plot) tissue shield interface with $N = 26$.

Monte Carlo Benchmarks

Using the external source and geometry defined in Fig. 3, the induced neutron and proton fluence spectra were evaluated at detector locations within the ICRU sphere by three MC codes (Geant4 [Agostinelli et al. 2003], FLUKA [Fasso et al. 2005, Battistoni et al. 2007], and PHITS [Sato et al. 2006, 2013]) and 3DHZETRN. Results are shown in Fig 9. The scoring regions (detectors) and physics options used in this set of simulations are identical to what was used in Wilson et al. [2014c, 2015] and will not be repeated here.

The proton fluence predictions among the three codes are in reasonable agreement above 1 MeV with very large statistical uncertainty below 1 MeV (not shown). Some of the differences in proton spectra at $z = 30$ may be associated with the simplified assumptions of the straight ahead approximation in 3DHZETRN light ion transport. The larger discrepancy lies with the neutron spectra, where disagreement among the MC results brackets the 3DHZETRN solution. The FLUKA and 3DHZETRN results exhibit a similar inflection in the neutron spectrum near 10 to 60 MeV that may be related to the use of an early FLUKA approximation to the secondary neutron spectrum used in HZETRN [Ranft 1980, Wilson et al. 1988] and carried over into 3DHZETRN.

To further quantify differences among the codes, the neutron spectra are converted into effective dose using conversion factors for isotropic neutrons evaluated by Pelliccioni [2000] using FLUKA. The effective dose on the top and bottom of the tissue sphere is given in Table 3. The 3DHZETRN ($N = 26$) compares well with the three MC codes, and is within 5% of the PHITS results. The older HZETRN ($N = 1$) provides a conservative overestimate as expected. An added measure of degree of agreement is to evaluate the relative root meant square (RMS) differences in the neutron fluence from the four codes as given in Table 4 on the top and the bottom of the ICRU sphere. Again, it is seen that the agreement of 3DHZETRN with the MC codes is about the same as the agreement of the MC codes among themselves.

A principle difference in the three codes is the computational efficiency. The time required by the three codes to run these benchmarks is given in CPU seconds used and listed in the first column of Table 5. Although it is difficult to favor one code over another on the basis of the veracity of the solutions obtained, there are vast differences in computational time required to evaluate fluence spectra even in this simplest of complex geometries (tissue sphere within a complex shield of a single elemental material). Still, Monte Carlo methods provide an important verification for developing codes capable of meeting operational and especially design requirements. Computational speed has proven to be important in spaceflight validation in low Earth orbit (LEO) where the time structure of the environment can be used to test various environmental components as was done using Liulin instrument measurements onboard the International Space Station (ISS) [Wilson et al. 2007, Slaba et al. 2013]. The main limitation on such studies remain the uncertainty in the environmental models (especially for the trapped environment) and uncertainty in nuclear cross sections.

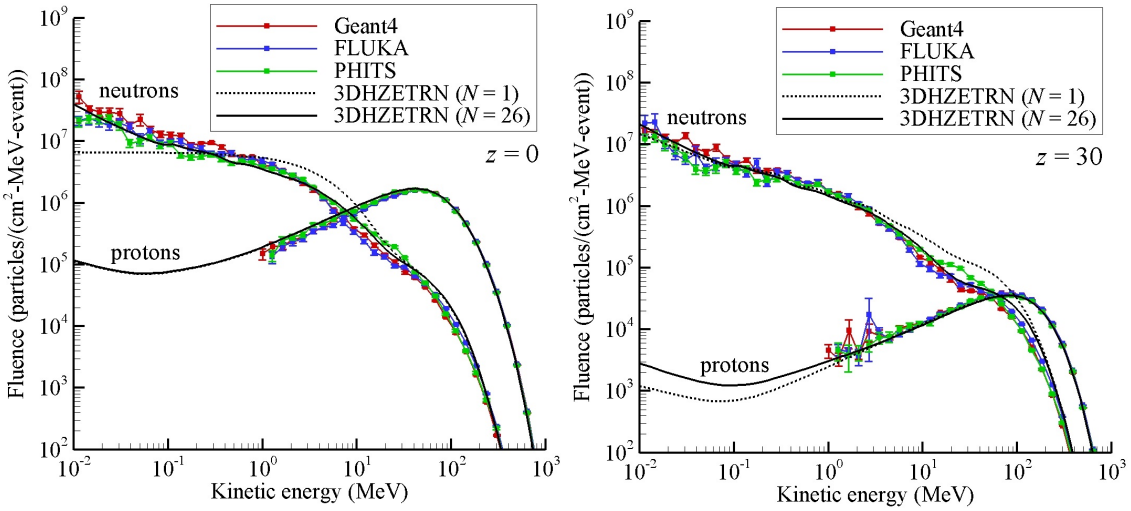

Fig. 9. Webber SPE benchmark with $N = 26$ compared with Geant4, FLUKA, and PHITS at detector locations near the top (left plot) and bottom (right plot) of the ICRU tissue sphere.

Table 3. Neutron effective dose values (mSv/event) at $z = 0$ g/cm^2 (top of ICRU sphere) and $z = 30$ g/cm^2 (bottom of ICRU sphere). Propagated MC statistical errors in neutron effective dose values were all less than 2%.

z (g/cm^2)	3DHZETRN ($N = 1$)	3DHZETRN ($N = 26$)	Geant4	FLUKA	PHITS
0	10.31	6.98	5.68	5.68	6.92
30	5.44	3.50	2.77	2.96	3.29

Table 4. Neutron fluence root mean square relative differences of 3DHZETRN ($N = 26$) and MC codes at $z = 0$ g/cm^2 (top of ICRU tissue sphere) and $z = 30$ g/cm^2 (bottom of ICRU sphere). Dimensionless units.

z (g/cm^2)	vs Geant4	vs FLUKA	vs PHITS	MC spread
0	0.468	0.308	0.269	0.676
30	0.433	0.327	0.339	0.674

Table 5. Total CPU seconds required for benchmark calculations. Total number of histories ran in Monte Carlo simulations are shown in parentheses.

	Webber SPE
3DHZETRN ($N = 26$)	59
Geant4	2.0×10^8 (3.5×10^{11})
FLUKA	5.1×10^8 (3.9×10^{11})
PHITS	9.6×10^7 (1.4×10^{11})

Conclusions

In this work, 3DHZETRN was extended to enable analysis of general combinatorial geometry. The extensions were tested by considering a cylindrical aluminum shell surrounding internal aluminum boxes and an ICRU tissue sphere. The internal boxes were positioned relative to the external source to provide only partial shielding of the ICRU sphere, thereby emphasizing 3D transport effects. Following the outline of previous studies [Wilson et al. 2014a-c, 2015], convergence tests were performed to determine the solution dependence on the number of transport directions, N. It was found that $N = 26$ provided nearly converged results with minimal relative error compared to the $N = 86$ solution.

Comparisons between 3DHZETRN and the MC codes, Geant4, FLUKA, and PHITS, were made at points within the geometry exposed to the Webber 1956 SPE. As in the previous studies [Wilson et al. 2014a-c, 2015], it was found that 3DHZETRN agrees well with MC codes. Most importantly, even within the complex geometry,

3DHZETRN was several orders of magnitude faster than the MC simulations. Future work will provide yet another extension to the 3DHZETRN geometry capabilities by enabling analysis through complex and realistic geometry described by only a single ray-trace thickness distribution. Such geometric descriptions are typically generated in the vehicle design and optimization process [Wilson et al. 2003, Walker et al. 2013], where detailed computer aided design models are maintained and developed [Qualls et al. 2001, Simon et al. 2014]. This extension is the critical step in connecting and integrating 3DHZETRN into shield optimization frameworks.

References

Agostinelli, S. et al., Geant4--a simulation toolkit. *Nucl. Instrum. & Methods A* **506**: 250-303; 2003.

Battistoni, G., Muraro, S., Sala, P.R., Cerutti, F., Ferrari, A., Roesler, S.,Fasso, A., Ranft, J., The FLUKA code: Description and benchmarking. *Proceedings of the Hadronic Shower Simulation Workshop 2006*, **896**: 31–49; 2007.

Fasso, A., Ferrari, A., Ranft, J., Sala, P.R., FLUKA: A multi-particle transport code, CERN-2005-10, INFN/TC 05/11, SLAC-R-773, 2005.

ICRU Internal Commission on Radiation Units and Measurements, *Quantities and Units in Radiation Protection Dosimetry*, ICRU Report 51, 1993.

Pelliccioni M., Overview of Fluence-to-Effective Dose and Fluence-to-Ambient Dose Equivalent Conversion Coefficients for High Energy Radiation Calculated Using the FLUKA Code. *Radiat. Prot. Dosim.* 88: 279-297; 2000.

Qualls, G.D., Wilson, J.W., Sandridge, C.A., Cucinotta, F.A., Nealy, J.E., Heinbockel, J.H., Hugger, C., Verhage, J., Anderson, B.M., Atwell, W., Zapp, N., Barber, R., International space station shielding model development. SAE ICES 2001-01-2370, 2001.

Ranft, J., The FLUKA and KASPRO hadronic cascade codes. *Computer Techniques in Radiation Transport and Dosimetry,* W. R. Nelson and T.M. Jenkins, eds, Plenum Press, 339-371; 1980

Sato, T., Niita, K., Iwase, H., Nakashima, H., Yamaguchi, Y., Sihver, L., Applicability of particle and heavy ion transport code PHITS to the shielding design of spacecrafts, *Rad. Meas.*, **41**: 1142 – 1146; 2006.

Sato, T., Niita, K., Matsuda, N., Hashimoto, S., Iwamoto, Y., Noda, S., Ogawa, T., Iwase, H.,Nakashima, H., Fukahori, T., Okumura, K., Kai, T., Chiba, S., Furuta T., Sihver, L., Particle and heavy ion transport code system PHITS, version 2.52, *J. Nucl. Sci. Technol.* **50**: 913-923; 2013.

Simon, M.A., Cerro J.A., Latorella, K., Clowdsley, M., Watson, J., Albertson, C., Norman, R., Le Boffe, V., Walker, S., Design of two RadWorks storm shelters for solar particle event shielding. AIAA Space 2014 Conference and Exposition, 2014.

Slaba, T.C., Blattnig, S.R., Badavi, F.F., Faster and more accurate transport procedures for HZETRN. *J. Comp. Phys.* **229**: 9397-9417; 2010a.

Slaba, T.C., Blattnig, S.R., Aghara, S.K., Townsend, L.W., Handler, T., Gabriel, T.A., Pinsky, L.S., Reddell, B., Coupled neutron transport for HZETRN. *Rad. Meas.* **45**: 173-182; 2010b.

Slaba, T.C., Blattnig, S.R., Reddell, B., Bahadori, A., Norman, R.B., Badavi, F.F., Pion and electromagnetic contribution to dose: Comparisons of HZETRN to Monte Carlo results and ISS data. *Adv. Space Res.* **52**: 62-78; 2013.

Walker, S.A., Clowdsley, M.S., Abston, H.L., Simon, M.A., Radiation exposure analysis supporting the development of solar particle event shielding technologies. 43rd International Conference on Environmental Systems, 2013.

Webber, W.R., An evaluation of solar-cosmic-ray events during solar minimum. D2-84274-1, Boeing Co., 1966.

Wilson, J.W., Analysis of the theory of high-energy ion transport. NASA TN-D-8381, 1977.

Wilson, J.W., Chun, S.Y., Buck, W.W., Townsend, L.W., High energy nucleon data bases. *Health Phys*., **55**: 817-819; 1988.

Wilson, J.W., Townsend, L.W., Schimmerling, W., Khandelwal, G.S., Khan, F., Nealy, J.E., Cucinotta, F.A., Simonsen, L.C., Shinn, J.L., Norbury, J.W., Transport methods and interactions for space radiations. NASA RP-1257, 1991.

Wilson, J.W., Korte, J.J., Sobieski, J., Badavi, F.F., Chokshi, S.M., Martinovic, Z.N., J. Cerro, J., Qualls, G.D., Radiation shielding, MDO processes, and single stage to orbit design, AIAA Space 2003, Sept 22, 2003, Long Beach, California, AIAA 2003-6259, 2003.

Wilson, J.W., Tripathi, R.K., Mertens, C.J., Blattnig, S.R., Clowdsley, M.S., Verification and validation: High charge and energy (HZE) transport codes and future development. NASA TP-2005-213784, 2005.

Wilson, J.W., Nealy, J.E., Dachev, Ts.P., Tomov, B.T., Cucinotta, F.A., Badavi, F.F., De Angelis, G., Atwell, W., Leutke, N., Time serial analysis of the induced LEO environment within the ISS 6A. *Adv. Space Res.* **40**(11): 1562-1570; 2007.

Wilson, J.W., Slaba, T.C., Badavi, F.F., Reddell, B.D., Bahadori, A.A., A 3DHZETRN code in a spherical uniform sphere with Monte Carlo verification. NASA TP-2014-218271, 2014a.

Wilson, J.W., Slaba, T.C., Badavi, F.F., Reddell, B.D., Bahadori, A.A., Advances in NASA space radiation research: 3DHZETRN, *Life Sci. Space Res.* **2**: 6-22; 2014b.

Wilson, J.W., Slaba, T.C., Badavi, F.F., Reddell, B.D., Bahadori, A.A., 3D space radiation transport in a shielded ICRU tissue sphere. NASA TP-2014-218530, 2014c.

Wilson, J.W., Slaba, T.C., Badavi, F.F., Reddell, B.D., Bahadori, A.A., 3DHZETRN: Shielded ICRU spherical phantom, *Life Sci. Space Res.* **4**: 46-61; 2015.

REPORT DOCUMENTATION PAGE

Form Approved
OMB No. 0704-0188

1. REPORT DATE *(DD-MM-YYYY)*	2. REPORT TYPE	3. DATES COVERED *(From - To)*
01- 11 - 2015	Technical Publication	

4. TITLE AND SUBTITLE

Solar Proton Transport within an ICRU Sphere Surrounded by a Complex Shield: Combinatorial Geometry

5a. CONTRACT NUMBER

5b. GRANT NUMBER

5c. PROGRAM ELEMENT NUMBER

6. AUTHOR(S)

Wilson, John W.; Slaba, Tony C.; Badavi, Francis F.; Reddell, Brandon D.; Bahadori, Amir A.

5d. PROJECT NUMBER

5e. TASK NUMBER

5f. WORK UNIT NUMBER

651549.02.07.10

7. PERFORMING ORGANIZATION NAME(S) AND ADDRESS(ES)

NASA Langley Research Center
Hampton, VA 23681-2199

8. PERFORMING ORGANIZATION REPORT NUMBER

L-20624

9. SPONSORING/MONITORING AGENCY NAME(S) AND ADDRESS(ES)

National Aeronautics and Space Administration
Washington, DC 20546-0001

10. SPONSOR/MONITOR'S ACRONYM(S)

NASA

11. SPONSOR/MONITOR'S REPORT NUMBER(S)

NASA/TP-2015-218980

12. DISTRIBUTION/AVAILABILITY STATEMENT

Unclassified - Unlimited
Subject Category 93
Availability: STI Program (757) 864-9658

13. SUPPLEMENTARY NOTES

14. ABSTRACT

The 3DHZETRN code, with improved neutron and light ion ($Z < 2$) transport procedures, was recently developed and compared to Monte Carlo (MC) simulations using simplified spherical geometries. It was shown that 3DHZETRN agrees with the MC codes to the extent they agree with each other. In the present report, the 3DHZETRN code is extended to enable analysis in general combinatorial geometry. A more complex shielding structure with internal parts surrounding a tissue sphere is considered and compared against MC simulations. It is shown that even in the more complex geometry, 3DHZETRN agrees well with the MC codes and maintains a high degree of computational efficiency.

15. SUBJECT TERMS

HZETRN; Radiation; Space

16. SECURITY CLASSIFICATION OF:			17. LIMITATION OF ABSTRACT	18. NUMBER OF PAGES	19a. NAME OF RESPONSIBLE PERSON
a. REPORT	b. ABSTRACT	c. THIS PAGE			STI Help Desk (email: help@sti.nasa.gov)
					19b. TELEPHONE NUMBER *(Include area code)*
U	U	U	UU	20	(757) 864-9658